Nat. Volatiles & Essent. Oils, 2021;08(1):152-166

NVEO
Natural Volatiles & Essential Oils

Exploration Of 4-Hydroxy-3-Nitrocoumarin: Spectroscopic Insights, Quantum Chemical Analysis, Molecular Docking, And Biological Evaluation As A Potent Bioactive Compound

Surya S. Mohan[1], M.R.Meera[2*], A. Rathika[3]

[1]Research scholar (Reg.No.20213092132012), Department of Physics, Muslim Arts College, Thiruvithancode-629174, Tamil Nadu, India. Affiliated to Manonmaniam Sundaranar University, Tirunelveli, Tamilnadu, India.
[2*]Department of Physics, Sree Ayyappa College for Women, Chunkankadai, Nagercoil-629 003, Tamil Nadu, India. Affiliated to Manonmaniam Sundaranar University, Tirunelveli, Tamilnadu, India.
[3]Department of Physics, Muslim Arts College, Thiruvithancode-629174, Tamil Nadu, India. Affiliated to Manonmaniam Sundaranar University, Tirunelveli, Tamilnadu, India.

***Corresponding Author**: Dr. M.R. Meera, Ph. D.,
Associate Professor, Department of Physics, Sree Ayyappa College for Women, Chunkankadai, Nagercoil 629 003, Tamil Nadu, India, TEL: +91-9443692523, Email: meeranairmrm17@gmail.com

Abstract
The 4-Hydroxy-3-nitrocoumarin compound underwent comprehensive characterization using FT-IR, FT-Raman, and UV-Vis spectroscopy. Computed vibrational wavenumbers were aligned with experimental values, revealing π to π* and n to π* electronic transitions. Analysis of frontier molecular orbitals, Molecular electrostatic potential surface, Mulliken atomic charge distribution, and Natural bond orbitals corroborated the compound's bioactivity, showcasing intramolecular charge transfer from the methyl group to the nitro group. Antibacterial testing confirmed activity against *Klebsiella pneumonia*. In vitro cytotoxicity studies demonstrated a stronger inhibition of A549 cancer cell lines compared to HeLa cells. Molecular docking analysis further supported these cytotoxicity findings. This research offers promising avenues for designing new drugs targeting lung cancer treatment.

Keywords: 4-Hydroxy-3-nitrocoumarin, DFT, Antibacterial, In vitro cytotoxicity, Molecular docking, Lung cancer drug.

1. Introduction

Coumarin, chemically identified as 2H-chromen-2-one with the formula C9H6O2, comprises a benzene molecule with adjacent hydrogen atoms replaced by unsaturated lactone rings (CH)=(CH)(C=O)O, forming a secondary six-membered heterocycle that shares carbon atoms with the benzene ring. Classified as a lactone and a member of the benzopyrone chemical class, coumarin is a colorless, tasteless crystalline substance with a scent reminiscent of vanilla sweetness [1,2]. This compound serves as a chemical defense in various plants, deterring predators. Methods for producing coumarin include the Perkin reaction using salicylaldehyde and acetic anhydride. Alternate pathways involve the Kostanecki acylation, utilized in producing chromones, and the Pechmann condensation, providing routes to coumarin and its derivatives. Medically, coumarin is employed in prescription medication like coumadin to prevent blood clot formation in cases of deep vein thrombosis, pulmonary embolism, and to mitigate atrial fibrillation-associated clotting, thrombotic strokes, and transient ischemic episodes. While coumarins have limited pharmaceutical

approval, their demonstrated biological activity, such as in treating lymphedema, presents potential for medical applications [3].

Cancer involves uncontrolled cell growth in the body, typically named after its initial site of development. Cervical cancer originates in the cervix, connecting the vagina and the upper uterus. It's more prevalent in individuals over 30. Persistent human papillomavirus (HPV) infection often leads to cervical cancer, a virus commonly transmitted through sexual activity. Despite around half of sexually active individuals encountering HPV, only a small percentage of women develop cervical cancer [4].

Efficient comprehension of biological molecules and drugs is achievable through computational molecular modeling tools like density functional theory (DFT) computations and molecular docking studies. DFT simulations elucidate a chemical system's reactivity, stable molecular structure, vibrational frequencies, charge transfer interactions, and potential reactive regions. These simulations, by defining local reactivity descriptors, facilitate comprehension of the interactions among beneficial molecular systems, thereby aiding the discovery of novel pharmacological compounds and the development of more potent drugs [5].

Molecular docking, a computer-based technique, evaluates the compatibility between a ligand and a receptor-binding site. It's a crucial tool in modern drug design, predicting binding mechanisms and affinities between a ligand and proteins. The integration of DFT quantum chemical calculations and molecular docking for the molecule 4-hydroxy-3-nitrocoumarin (4H3NC) sets the stage for subsequent in vivo research on this compound. Notably, antibacterial and in vitro anticancer investigations have gained significant relevance in novel drug development [6].

In this study, DFT quantum chemical computations were conducted using the Gaussian 09W software package and the B3LYP functional method. Comparative analyses were performed between the experimental Fourier transform-infrared (FT-IR) and Fourier transform-Raman (FT-Raman) spectra of 4-hydroxy-3-nitrocoumarin (4H3NC) and the computed infrared and Raman spectra of the molecule. Theoretical UV-Vis spectra were generated and compared with experimental UV-Vis spectra. Additionally, DFT computations included assessments of Mulliken atomic charge distribution, frontier molecular orbitals, and Natural bond orbitals. The compound's antibacterial and in vitro anticancer properties were investigated, and the anticancer findings were corroborated through molecular docking analysis [7].

2. Materials and Methods

2.1 Experimental characterizations

The 99% pure 4H3NC chemical was procured from Sigma-Aldrich Chemicals Co. in St. Louis, Missouri, United States. Experimental spectra, including Fourier transform-infrared (FT-IR) and Fourier transform-Raman (FT-Raman), were obtained using a Perkin Elmer Spectrum 1 FT-IR spectrometer employing a KBr pellet technique at room temperature, achieving a resolution of 1.0 cm^{-1}. The recorded FT-IR and FT-Raman spectra encompassed the wavenumber range of 3500-400 cm^{-1}. Additionally, the FT-Raman spectrum was captured utilizing a BRUKER RFS 27 Stand-alone Raman spectrometer at room temperature, offering a resolution of 2 cm^{-1}. The UV-Vis spectrum was acquired using a Shimadzu UV-3600 ultraviolet (UV) visible Near Infrared spectrophotometer, employing ethanol as the solvent and capturing the spectrum in the range of 200-600 nm.

2.2 Computational details

The Gaussian 09W software and the DFT/B3LYP method with the cc-pVTZ basis set were employed to optimize the chemical structure of the 4H3NC molecule [8]. This method facilitated the determination of the most stable molecular configuration for 4H3NC. Subsequently, the computed vibrational wavenumbers and their assignments were analyzed using the VEDA 4.0 program. To simulate the UV-visible spectrum of 4H3NC in an ethanol environment, the TD-DFT/B3LYP approach coupled with the polarizable continuum model (PCM) was utilized. Visualizations of the computed data, including vibrational wavenumbers, UV-Vis spectra, Mulliken atomic charge distribution, and FMOs, were generated using the GaussView 05

visualization software [9]. It's noteworthy that all computations were performed at the ground state energy level of the 4H3NC molecule without imposing restrictions on the potential energy surface.

3. Results and discussion

3.1 Molecular geometry and symmetry

The 4H3NC molecule underwent optimization using the DFT/B3LYP approach with the cc-pVTZ basis set, revealing a global minimum energy value of −777.03 a.u. (atomic units), as depicted in Figure 1. Detailed bond lengths, bond angles, and dihedral angle values for the molecule are outlined in Table 1. Notably, the 4H3NC molecule displays C1 point group symmetry, confirming its non-centrosymmetric nature. Analysis of the vibrational wavenumbers observed in both IR and Raman spectra further supports this molecular structure. The presence of partial bonds within the molecule implies electron transfers, heightening its bioactivity. Moreover, the absence of negative vibrational wavenumbers indicates the improved stability of the 4H3NC molecule due to its refined molecular configuration [10].

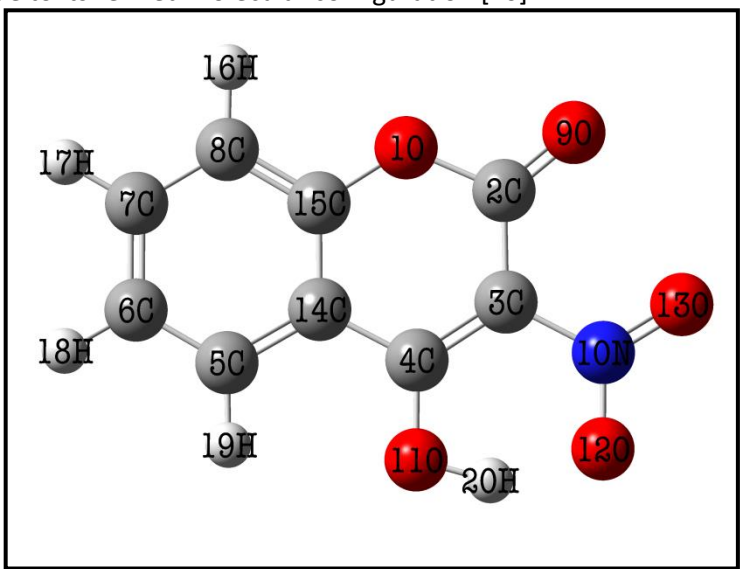

Fig. 1. Optimized molecular structure of 4-Hydroxy-3-nitrocoumarin molecule

Table 1. The calculated structural parameters of 4-Hydroxy-3-nitrocoumarin molecule

Structural Parameters	cc-pVTZ	Structural Parameters	cc-pVTZ	Structural Parameters	cc-pVTZ
Bond Length (Å)		**Bond Angle (Degree)**		**Dihedral Angle (Degree)**	
O1-C2	1.3901	C6-C5-H19	118.29	C2-C3-N10-O12	179.70
O1-C15	1.4145	C14-C5-H19	120.85	C2-C3-N10-O13	−0.25
C2-C3	1.4674	C5-C6-C7	120.49	C4-C3-N10-O12	0
C2-O9	1.2250	C5-C6-H18	119.68	C4-C3-N10-O13	−179.96
C3-C4	1.3364	C7-C6-H18	119.82	C3-C4-O11-H20	0
C3-N10	1.4260	C6-C7-C8	119.72	C14-C4-O11-H20	179.50
C4-O11	1.3760	C6-C7-H17	120.09	C3-C4-C14-C5	177.77
C4-C14	1.4710	C8-C7-H17	120.17	C3-C4-C14-C15	−1.48
C5-C6	1.4007	C7-C8-C15	119.17	O11-C4-C14-C5	−1.77
C5-C14	1.4015	C7-C8-H16	120.04	O11-C4-C14-C15	178.96
C5-H19	1.0875	C15-C8-H16	120.77	C14-C5-C6-C7	0.25
C6-C7	1.3935	C3-N10-O12	117.09	C14-C5-C6-H18	−179.76
C6-H18	1.0865	C3-N10-O13	117.10	H19-C5-C6-C7	−179.99
C7-C8	1.3900	O12-N10-O13	125.80	H19-C5-C6-H18	-0.00
C7-H17	1.0859	C4-O11-H20	109.13	C6-C5-C14-C4	−179.99
C8-C15	1.3964	C4-C14-C5	124.70	C6-C5-C14-C15	-0.73
C8-H16	1.0859	C4-C14-C15	118.01	H19-C5-C14-C4	0.25

N10-O12	1.2370	C5-C14-C15	117.27	H19-C5-C14-C15	179.52
N10-O13	1.2371	O1-C15-C8	116.10	C5-C6-C7-C8	0.23
O11-H20	0.9714	O1-C15-C14	121.40	C5-C6-C7-H17	179.98
O12-H20	1.6354	C8-C15-C14	122.48	H18-C6-C7-C8	−179.75
C14-C15	1.4003	**Dihedral Angle (Degree)**		H18-C6-C7-H17	−0.00
Bond Angle (Degree)		C15-O1-C2-C3	−1.50	C6-C7-C8-C15	−0.20
C2-O1-C15	122.11	C15-O1-C2-O9	178.79	C6-C7-C8-H16	179.57
O1-C2-C3	114.83	C2-O1-C15-C8	−178.56	H17-C7-C8-C15	−179.95
O1-C2-O9	121.88	C2-O1-C15-C14	0.91	H17-C7-C8-H16	−0.17
C3-C2-O9	123.28	O1-C2-C3-C4	0.60	C7-C8-C15-O1	179.16
C2-C3-C4	125.36	O1-C2-C3-N10	−179.08	C7-C8-C15-C14	−0.31
C2-C3-N10	116.44	O9-C2-C3-C4	−179.70	H16-C8-C15-O1	−0.61
C4-C3-N10	118.18	O9-C2-C3-N10	0.61	H16-C8-C15-14	179.91
C3-C4-O11	127.02	C2-C3-C4-O11	−179.62	C4-C14-C15-O1	0.63
C3-C4-C14	118.23	C2-C3-C4-C14	0.88	C4-C14-C15-C8	−179.91
O11-C4-C14	114.73	N10-C3-C4-O11	0.04	C5-C14-15-O1	−178.67
C6-C5-C14	120.84	N10-C3-C4-C14	−179.43	C5-C14-C15-C8	0.77

3.2 Vibrational spectral analysis

The optimized structure of the 4H3NC molecule comprises 20 atoms and demonstrates C1 point group symmetry, presenting a total of 54 normal vibrational modes. Table 2 contains detailed vibrational frequencies, IR intensities, Raman scattering activities, and corresponding assignments for the 4H3NC molecule. To align the calculated vibrational frequencies with experimental measurements and accommodate for anharmonicity in DFT computations, scaling factors were applied. Utilizing the formula $C = \Sigma(v_i * \omega_i)/\Sigma\omega_i^2$, specific scaling factors of 0.9622 for stretching and 0.9991 for bending vibrational modes were employed. Figures 2 and 3 illustrate the infrared and Raman spectra of the 4H3NC molecule, respectively, showcasing a slight deviation of around 8% between calculated and experimental values [11,12].

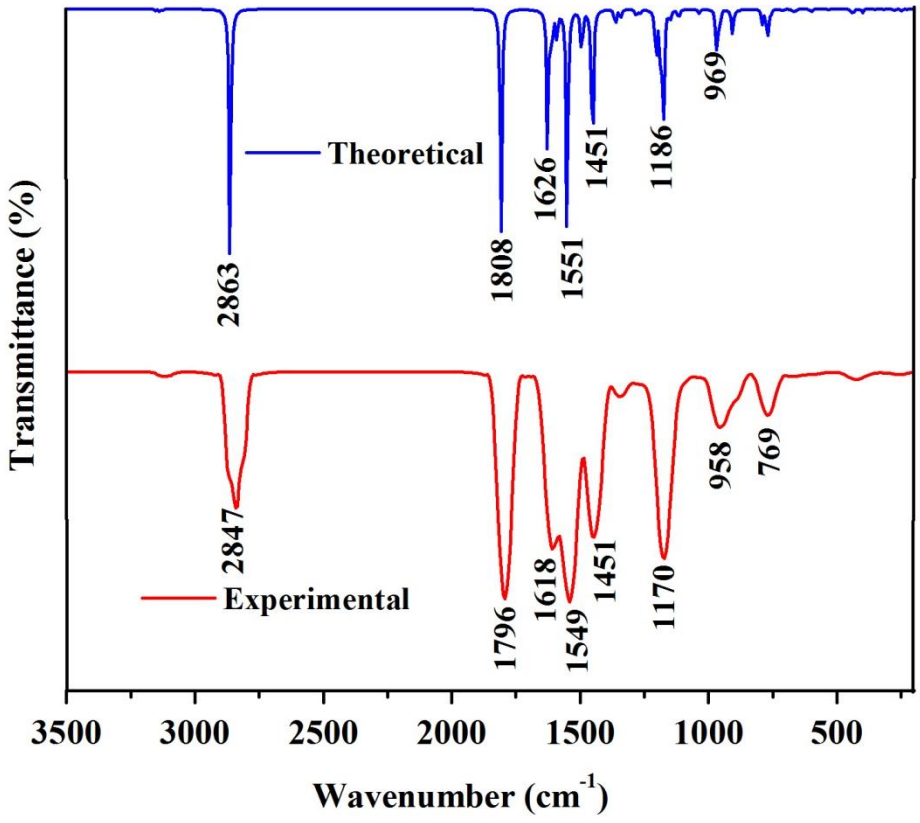

Fig. 2. Infrared spectra of 4-Hydroxy-3-nitrocoumarin molecule

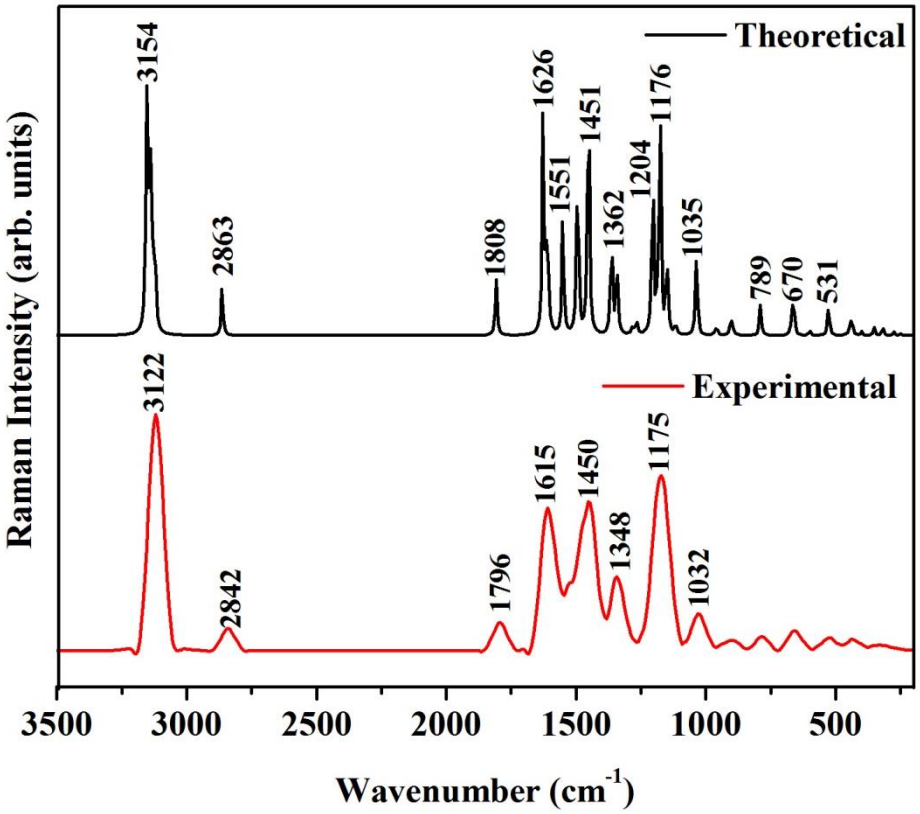

Fig. 3. Raman spectra of 4-Hydroxy-3-nitrocoumarin molecule

Table 2. The detailed observed and calculated vibrational frequencies, IR intensities, Raman scattering activities, and corresponding assignments for the 4H3NC molecule.

S. No	Observed Wavenumber (cm^{-1})		Wavenumber (cm^{-1})		IR Intensity (Km mol^{-1})	Raman scattering activity (Å^4 amu^{-1})	Reduced Mass (amu)	Force Constant (mDyne/Å^{-1})	Assignment with PED (%)
	FT-IR	FT-Raman	Calculated	Scaled					
1	-	3122vs	3215	3154	3.69	171.34	1.09	6.67	CH stretching (98)
2			3209	3148	0.64	107.69	1.09	6.64	CH stretching (97)
3			3197	3136	5.39	155.64	1.09	6.57	CH stretching (96)
4			3181	3121	2.82	76.98	1.09	6.49	CH stretching (97)
5	2847 vs	2842m	2918	2863	534.99	38.23	1.07	5.37	OH stretching (96)
6	1796 vs	1796m	1843	1808	520.99	38.12	13.13	26.26	C=O CH stretching (79)
7	1618 s	1615vs	1658	1626	288.15	127.37	4.7	7.61	CC stretching (34) + CH in plane bending (23)
8			1642	1611	80.71	65.87	4.61	7.32	CC stretching (43) + OH in plane bending (21)
9			1622	1591	69.1	1.52	5.18	8.03	CC stretching (21) + OH in plane bending (22)
10	1549 vs		1581	1551	486.29	68.93	5.7	8.39	CC stretching (33) + NO_2 stretching (12)
11			1523	1494	102.21	99.88	3.12	4.27	CH in plane bending (11)

12			1483	1455	92.2	42.89	2.27	2.94	CH in plane bending (34) + OH in plane bending (12)
13	1451 vs	1450vs	1479	1451	261.16	112.08	4.86	6.26	CH in plane bending (54)
14	-	1348s	1389	1362	36.59	58.66	2.76	3.13	CH in plane bending (34) + OH in plane bending (21)
15			1368	1342	22.37	42.58	6.47	7.13	CH in plane bending (54)
16			1306	1281	15.19	5.35	1.91	1.92	CC stretching (25) + OH in plane bending (34)
17			1290	1265	9.94	7.37	4.19	4.11	CH in plane bending (44) + OH in plane bending (12)

S. No.	Observed Wavenumber (cm^{-1})		Wavenumber (cm^{-1})		IR Intensity (Km mol^{-1})	Raman scattering activity ($Å^4$ amu^{-1})	Reduced Mass (amu)	Force Constant (mDyne/$Å^{-1}$)	Assignment with PED (%)
	FT-IR	FT-Raman	Calculated	Scaled					
18			1228	1204	116.14	92.82	4.2	3.73	CH in plane bending (12)
19			1209	1186	102.84	10.3	2.23	1.92	CH in plane bending (23)+ OH in plane bending (11)
20	1170vs	1175vs	1199	1176	245.24	120.05	3.62	3.07	CH in plane bending (13)
21			1172	1149	21.7	42.83	1.68	1.36	CH in plane bending (24)
22			1137	1115	19.65	5.8	2.01	1.53	CH in plane bending (43)
23		1032m	1055	1035	9.77	41.07	2.06	1.35	CH out of plane bending (21)
24			1015	995	0.46	0.05	1.32	0.8	CH out of plane bending (33)
25			991	972	1.61	0.1	1.33	0.77	OH out of plane bending (22)
26	958m	-	988	969	76.56	0.63	1.1	0.63	CO stretching (12)
27			977	958	47.96	4.67	11.65	6.55	Ring breathing (14)
28			925	907	51.54	3.74	7.38	3.72	Ring breathing (15)
29			915	897	10.65	7.17	7.16	3.54	CH out of plane bending (44)
30			896	879	1.43	0.42	1.51	0.71	NO_2 in plane bending (64)
31			805	789	27.72	12.94	10.61	4.05	CH out of plane bending (22)
32			804	788	0.39	1.09	4.68	1.78	CH out of plane bending (33)
33	769m	-	786	771	68.36	0.28	1.89	0.69	CH out of plane bending (33)
34			772	757	11.17	0.02	2.98	1.05	CH out of plane bending (12)
35			725	711	4.1	0.02	12.07	3.73	CH out of plane bending (22)
36			686	673	1.85	1.59	8.12	2.25	CH out of plane bending (22)

S. No.	Observed Wavenumber (cm^{-1})		Wavenumber (cm^{-1})		IRIntensity (Km mol^{-1})	Raman scattering activity ($Å^4$ amu^{-1})	Reduced Mass (amu)	ForceConstant (mDyne/$Å^{-1}$)	Assignment with PED (%)
	FT-IR	FT-Raman	Calculated	Scaled					
37			683	670	0.56	0.31	4.99	1.37	CH out of plane bending (33)
38			676	663	7	20.02	7.04	1.9	CH out of plane bending (54)
39			611	599	6.97	2.32	8.65	1.9	Ring vibration (11)
40			542	531	2.07	0.32	3.4	0.59	Ring vibration (24)
41			537	526	0.01	12.99	10.39	1.77	CCCC bending (21), COCO bending (36)
42			455	446	4.01	2.93	12.05	1.47	CCNO bending (45)
43			445	436	7.12	7.94	9.74	1.14	CH out of plane bending (11)
44			445	436	4.33	0.19	3.55	0.41	CCOH in bending (23)
45			407	399	7.75	1.8	6.25	0.61	Ring vibration (33)
46			358	351	1.2	3.3	9.24	0.7	Ring vibration (12)
47			324	317	1.44	3.33	10.8	0.67	Ring vibration (26)
48			280	274	2.98	1.49	6.23	0.29	Ring vibration (42)
49			254	249	3.85	0.65	9.92	0.38	Ring vibration (11)
50			228	223	1.05	0.09	7.16	0.22	Ring vibration (23)
51			165	161	0.03	1.67	6.59	0.11	Ring vibration (12)
52			91	89	0.07	0.67	9.16	0.04	Ring torsion (11)
53			76	74.5712	0.19	0.43	7.11	0.02	Ring torsion (10)
54			28	27.4736	0.11	0.52	12.77	0.01	Ring torsion (13)

3.3 UV-Visible analysis

UV-visible spectrum analysis is a powerful tool for understanding the electronic properties of organic compounds, offering insights into their behavior in different states. In this case, the experimental UV-visible spectrum of the 4H3NC molecule was captured in a liquid ethanol environment, while the simulated UV-visible spectrum was generated using the TD-DFT method with the B3LYP/cc-pVTZ basis set. Fig. 4 illustrates both the predicted and observed UV-visible spectra of the 4H3NC molecule, while Table 3 outlines essential details like excitation wavelength (λ), excitation energy (E), oscillator strength (f), and corresponding orbital contributions, shedding light on its electronic transitions [13].

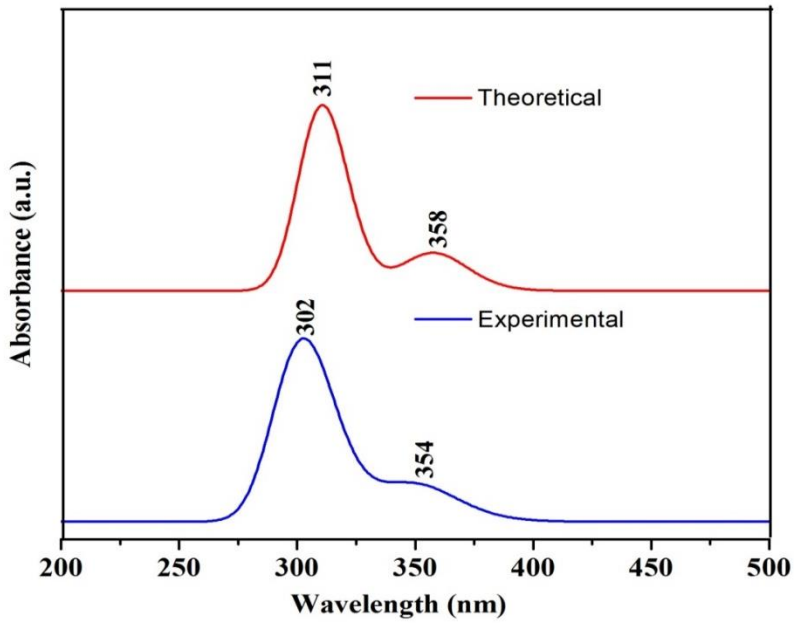

Fig. 4. Simulated and observed UV-visible spectra of the 4H3NC molecule

Table 3. The calculated and observed UV-Vis spectral parameters in ethanol solution for 4H3NC molecule with its assignments.

Calculated				**Observed**		**Assignment**
λ (nm)	E (eV)	f	Orbital contribution	λ (nm)	E (eV)	
311	3.99	0.20	H-1→L (97%)	302	4.11	π→π*
358	3.46	0.11	H→L (98%)	354	3.50	n→π*

3.4. Mulliken atomic charge distribution analysis

The distribution of Mulliken atomic charges in a molecule significantly influences its dipole moment and polarizability. In this investigation, the DFT/B3LYP method, coupled with the cc-pVTZ basis set, was employed to simulate the Mulliken atomic charge distribution of the 4H3NC molecule. Fig. 5 depicts the resulting Mulliken atomic charge distribution. Notably, carbon atom C14 (0.734) exhibits an unusually high positive charge due to its bonding with the electronegative oxygen atoms O11 and O10. Conversely, oxygen atom O1 (−0.588) demonstrates a considerable negative charge. The molecule showcases a pattern where electronegative atoms carry negative charges, while hydrogen atoms bear positive charges. Interestingly, hydrogen atom H24 (0.192) appears to contribute electrons to carbon atom C16, supported by similar trends in the neighboring hydrogen atoms H25 and H26 in the methyl group, having values of 0.217. Furthermore, the negative charge values observed in carbon atoms C15 (0.156) and C16 (0.579) suggest electron donation from oxygen atom O10 and hydrogen atom H24, initiating a delocalization of charges within the molecule, underscoring its bioactive nature [14].

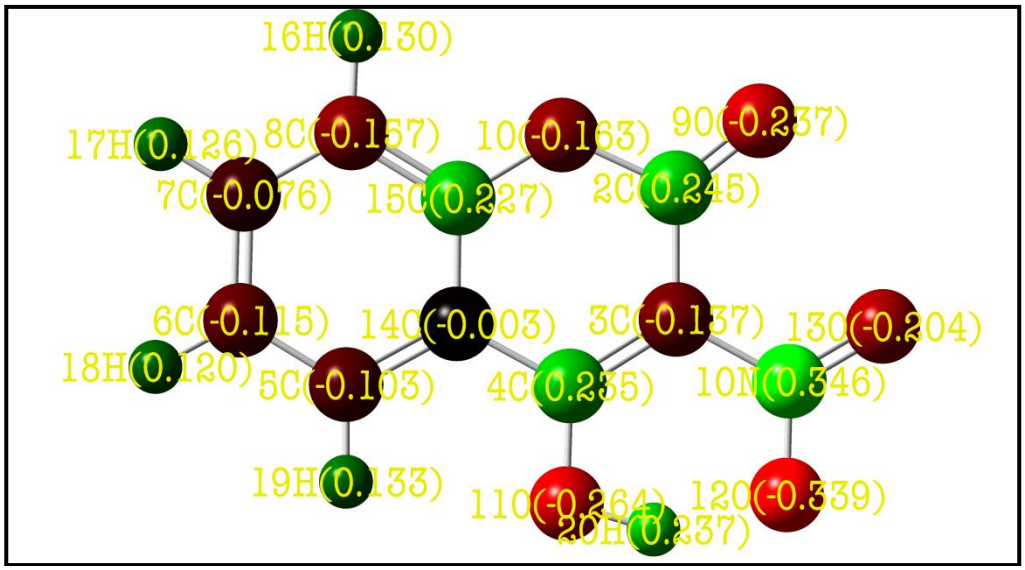

Fig. 5. Mulliken atomic charge distributions of 4-Hydroxy-3-nitrocoumarin molecule

3.5. Frontier molecular orbitals (FMOs) analysis

Frontier molecular orbitals (FMOs) serve as a key tool to understand a molecule's reactivity and its interactions with other molecules. Typically, Koopmans' theorem guides FMO analysis, elucidating chemical potential, hardness, electrophilicity, and electronegativity of organic compounds. A molecule with a narrow energy gap signifies higher reactivity and polarization. Fig. 6 illustrates the simulated FMOs for the 4H3NC molecule, where red and green depict positive and negative phases, respectively. Table 4 presents insights into HOMO and LUMO energies, the energy gap, and other FMO-related chemical characteristics of the 4H3NC molecule. The determined energy gap of 4.03 eV for the 4H3NC molecule indicates its most stable structure.

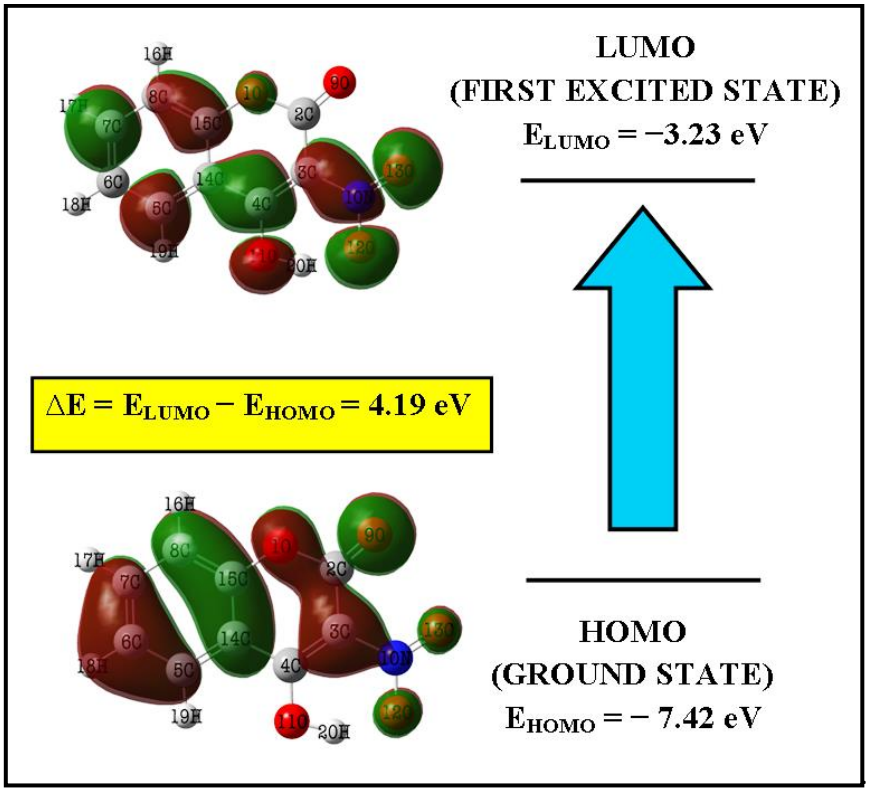

Fig. 6. FMOs of 4-Hydroxy-3-nitrocoumarin molecule

Table 4. The calculated FMOs-related molecular properties of the 4H3NC molecule

Molecular properties	Energy (eV)
E_{HOMO}	− 7.42
E_{LUMO}	− 3.23
Energy gap	4.19
Ionization energy (I)	7.42
Electron Affinity (A)	3.23
Global hardness (η)	2.09
Global Softness (S)	0.48
Chemical potential (μ)	−5.32
Electrophilicity index (ω)	6.77

This value aligns with band gap energies of reported bioactive chemicals. Moreover, the high ionization energy of 7.42 eV suggests resistance to nucleophilic attack, contributing to its stability. The molecule's robustness is supported by higher hardness (2.02 eV) and lower softness (0.49 eV) values. The calculated electrophilicity index of 6.61 eV underscores its enhanced electrophilic nature, correlating with its bioactivity [15].

3.6 Natural bond orbital analysis

The NBO analysis, conducted through the DFT/B3LYP approach using the cc-pVTZ basis set and NBO 3.1 programme integrated into Gaussian 09 software, offered valuable insights into the molecule's hydrogen bonding and intra- as well as intermolecular charge transfer interactions. Table 5 presents the stabilisation energy E(2) associated with the delocalization of individual donor (i) to acceptor (j) pairs, as determined by second-order Fock matrix perturbation theory. These values shed light on intramolecular charge transfer (ICT) and the formation of hydrogen bonds within the molecule, elucidating the energy differences between interacting orbitals of the donors and acceptors. Notably, the increased stabilization primarily arises from transitions involving the molecule's LP of O12 to π*(N10-O13), LP of O11 to π*(C3-C4), and LP of O12 to σ*(O11-H20). Such stabilization interactions, common in medicinal substances, signify a link between LP

orbitals and anti-bonding orbitals, indicating enhanced reactivity and bioactivity due to ICT within the molecule [16].

Table 5. Second order perturbation theory analysis of Fock matrix of 4-Hydroxy-3-nitrocoumarin molecule by natural bond orbital analysis.

Donor (i)	ED (i) e	Acceptor (j)	ED (j) e	E (2)[a] (Kcal/mol)	E(j)-E(i)[b] (a.u)	F(i,j)[c] (a.u)
σ(C2-C3)	1.9791	σ*(C4-O11)	0.0169	4.01	1.10	0.05
σ(C3-C4)	1.9822	σ*(C5-C14)	0.0199	3.16	1.26	0.05
π(C3-C4)	1.7018	π*(C2-O9)	0.2690	27.52	0.31	0.08
π(C3-C4)	1.7018	π*(C3-C4)	0.3631	5.76	0.28	0.03
π(C3-C4)	1.7018	π*(N10-O13)	0.5881	34.43	0.17	0.07
π(C3-C4)	1.7018	π*(C14-C15)	0.4336	7.72	0.30	0.04
σ(C4-C14)	1.9721	σ*(C3-N10)	0.0955	4.01	0.99	0.05
π(C5-C6)	1.6898	π*(C7-C8)	0.2921	21.94	0.28	0.07
π(C5-C6)	1.6898	π*(C14-C15)	0.4336	16.83	0.27	0.06
σ(C5-C14)	1.9728	σ*(O1-C15)	0.0340	4.05	1.06	0.05
σ(C5-H19)	1.9749	σ*(C6-C7)	0.0153	4.49	1.05	0.06
σ(C5-H19)	1.9749	σ*(C14-C15)	0.0371	5.35	1.04	0.06
σ(C6-H18)	1.9756	σ*(C5-C14)	0.0199	4.89	1.03	0.06
σ(C6-H18)	1.9756	σ*(C7-C8)	0.0120	4.36	1.06	0.06
σ(C7-C8)	1.9797	σ*(O1-C15)	0.0340	4.28	1.08	0.06
π(C7-C8)	1.6779	π*(C5-C6)	0.2716	16.17	0.29	0.06
π(C7-C8)	1.6779	π*(C14-C15)	0.4336	24.66	0.27	0.07
σ(C7-H17)	1.9763	σ*(C8-C15)	0.0214	4.67	1.05	0.06
σ(C8-H16)	1.9747	σ*(C6-C7)	0.0153	4.25	1.05	0.06
σ(C8-H16)	1.9747	σ*(C14-C15)	0.0371	4.78	1.04	0.06
π(N10-O13)	1.9868	π*(N10-O13)	0.5881	6.55	0.33	0.04
σ(O11-H20)	1.9823	σ*(C4-C14)	0.0334	7.24	1.19	0.08
π(C14-C15)	1.6080	π*(C3-C4)	0.3631	26.01	0.26	0.07
π(C14-C15)	1.6080	π*(C5-C6)	0.2716	19.44	0.30	0.07
π(C14-C15)	1.6080	π*(C7-C8)	0.2921	14.07	0.30	0.05
LP (1) O1	1.9551	σ*(C2-C3)	0.0776	5.65	0.97	0.06
LP (1) O1	1.9551	σ*(C14-C15)	0.0371	8.31	1.08	0.08
LP (2) O1	1.7525	π*(C2-O9)	0.2690	33.53	0.35	0.09
LP (2) O1	1.7525	π*(C14-C15)	0.4336	33.21	0.34	0.10
LP (2) O9	1.8096	σ*(O1-C2)	0.1321	38.84	0.55	0.13
LP (2) O9	1.8096	σ*(C2-C3)	0.0776	23.28	0.66	0.11
LP (1) O11	1.9679	σ*(C3-C4)	0.0361	9.67	1.11	0.09
LP (2) O11	1.7447	π*(C3-C4)	0.3631	55.71	0.32	0.12
LP (1) O12	1.9697	σ*(C3-N10)	0.0955	7.77	1.02	0.08
LP (1) O12	1.9697	σ*(O11-H20)	0.1008	5.52	1.09	0.07
LP (2) O12	1.8461	σ*(C3-N10)	0.0955	4.56	0.66	0.05
LP (2) O12	1.8461	σ*(N10-O13)	0.0431	16.75	0.81	0.10
LP (2) O12	1.8461	σ*(O11-H20)	0.1008	42.62	0.72	0.15
LP (3) O12	1.5902	π*(N10-O13)	0.5881	109.33	0.16	0.12
LP (1) O13	1.9798	σ*(C3-N10)	0.0955	4.85	1.07	0.06
LP (2) O13	1.8754	σ*(C3-N10)	0.0955	17.87	0.57	0.09
LP (2) O13	1.8754	σ*(N10-O12)	0.0757	23.33	0.63	0.10

3.7 Molecular electrostatic potential surface analysis

The MEP analysis of the 4H3NC molecule, as depicted in Fig. 7, offers a visual representation of its chemically active sites. The MEP surface's color scheme, ranging from red (electron-rich) to blue (electron-deficient), signifies the molecule's electron density variations. Surrounding the oxygen atoms, indicated by red areas, lies electron-rich zones due to the lone pair. Conversely, the hydrogen atoms H16, H17, H18, H19, and H20 reside within electron-deficient (blue) regions in the 4H3NC molecule. A neutral electrostatic potential area (green) encompasses the coumarin ring. Based on the MEP analysis, the vicinity encompassing the oxygen atom O9 and the hydrogen atom H18 are identified as potential sites for electrophilic and nucleophilic attacks, respectively [17].

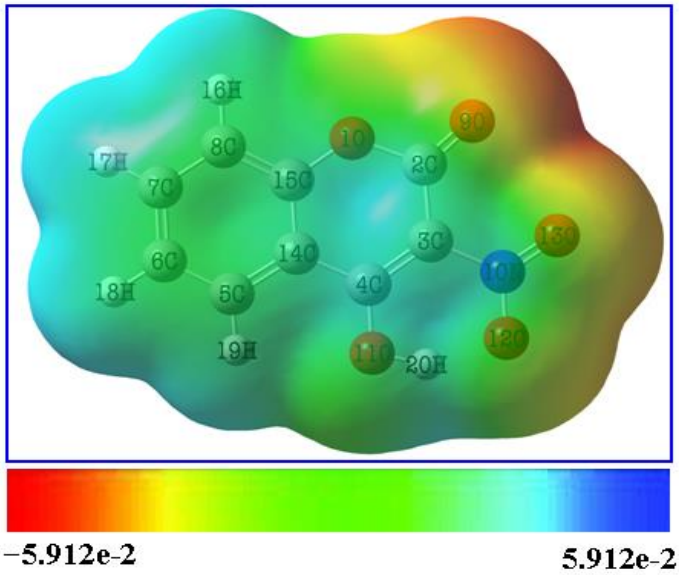

Fig. 7. Molecular Electrostatic Potential Surface of 4H3NC molecule

3.8 Antibacterial analysis

The experimental evaluation of the 4H3NC compound's antibacterial activity was conducted via the well diffusion method. The compound was subjected to testing against four bacterial strains: *Staphylococcus aureus, Klebsiella pneumoniae, Escherichia coli, and Pseudomonas aeruginosa* [18]. The results, depicted in Fig. 8 and summarized in Table 6, highlight the diameters of inhibitory zones observed for the 4H3NC compound against these bacterial strains. Notably, the findings affirm that the 4H3NC molecule demonstrates a more pronounced inhibitory effect specifically on *Klebsiella pneumoniae* in comparison to the other bacteria tested.

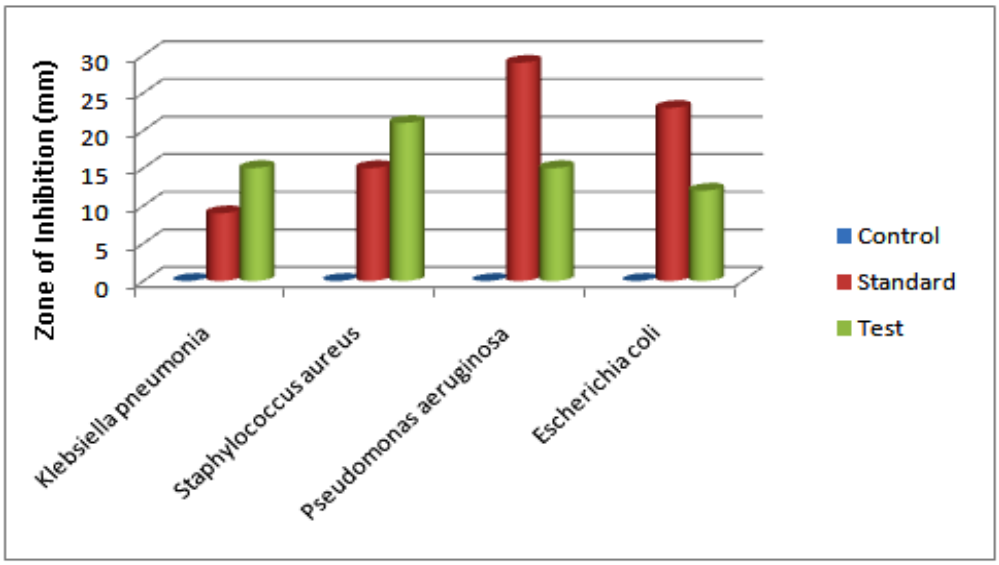

Fig. 8. Diameters of inhibitory zones for the 4H3NC compound against the four bacterial strains (a) *Klebsiella pneumonia*, (b) *Staphylococcus aureus*, (c) *Pseudomonas aeruginosa* and (d) *Escherichia coli*

Table 6. Diameters of inhibitory zones (mm) for 4H3NC compound against four bacterial strains

Bacterial Strains	Zone of Inhibition (mm)		
	Control	Standard	Test
Klebsiella pneumonia	NIL	9	15
Staphylococcus aureus	NIL	15	21
Pseudomonas aeruginosa	NIL	29	15
Escherichia coli	NIL	23	12

3.9 In vitro cytotoxicity assay for anticancer activity

MTT assay

The cytotoxicity impact of the 4H3NC compound was assessed using the MTT assay on HeLa (cervical) and A549 (lung) cancer cell lines. The cells were exposed to concentrations of 4H3NC ranging from 0-360 µg/ml for 24 hours [19,20]. The viability of HeLa and A549 cell lines following exposure to varying concentrations of 4H3NC is depicted in Figs. 9 and 10, respectively. Notably, after a 24-hour exposure, the viability of A549 cells decreased to around 20% at a concentration of 300 µg/ml of 4H3NC. Similarly, HeLa cell viability reduced to about 25% after 24 hours of treatment with 4H3NC at a concentration of 375 µg/ml.

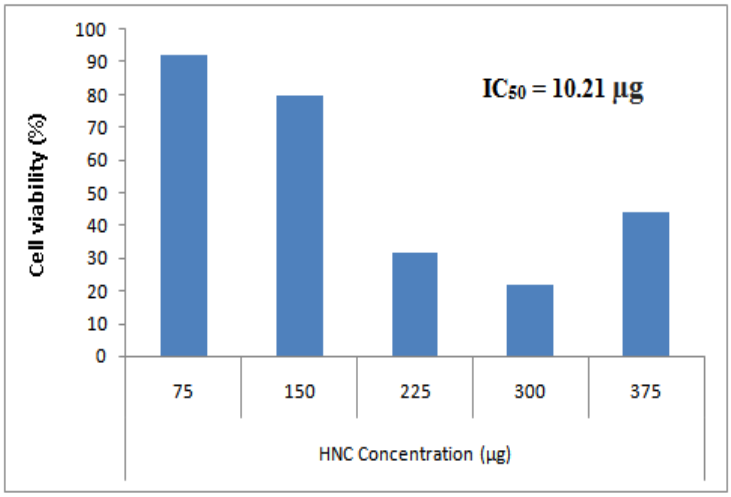

Fig.9. MTT assay measurement on different percentages of cell viability in A549 lung cancer cell lines against varied concentrations of 4H3NC compound.

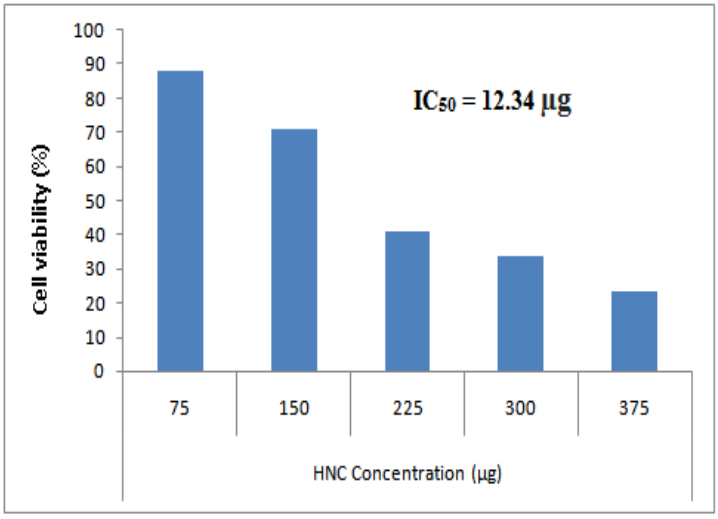

Fig.10. MTT assay measurement on different percentages of cell viability in HeLa cervical cancer cell lines against varied concentrations of 4H3NC compound

The calculated IC_{50} values for the 4H3NC compound were 10.21 µg/ml for the A549 lung cancer cell line and 12.34 µg/ml for the HeLa cervical cancer cell line. These findings suggest that the 4H3NC compound exhibits

a more potent inhibitory effect on the proliferation of A549 lung cancer cells compared to HeLa cervical cancer cells. Fig. 11 presents images of the control and treated A549 and HeLa cancer cell lines with the 4H3NC compound, showcasing noticeable morphological changes such as cell swelling and rupture. These observations hint at the potential effectiveness of the 4H3NC compound as a promising treatment for lung cancer.

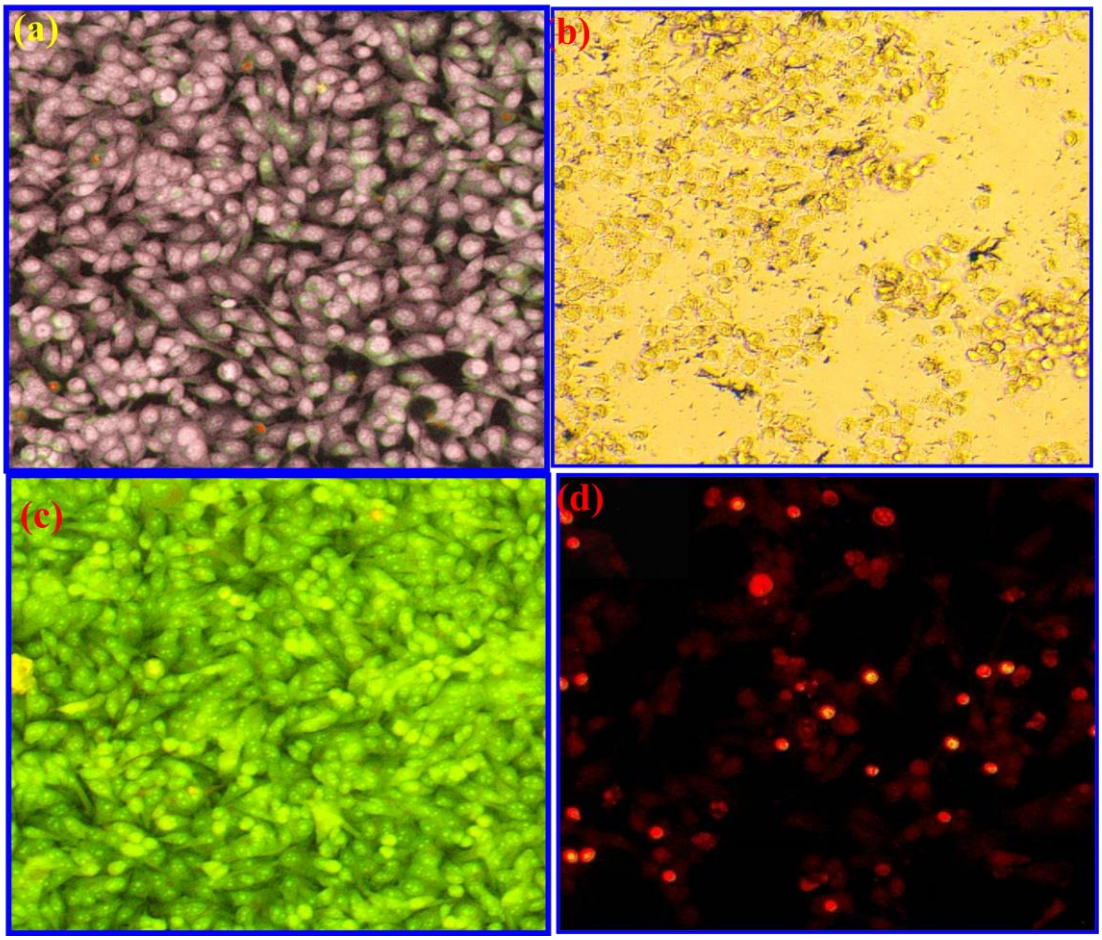

Fig.11. Morphological profile of the A549 cells (a) control and (b) after treated with HNC compound for 24 hours and the morphological profile of the HeLa cells (c) control and (d) after treated with HNC compound for 24 hours.

3.10 Molecular docking analysis

Molecular docking is a powerful tool in drug development, exploring the relationship between a molecule's structure and its activity. It predicts key characteristics like binding energy, inhibition constants, and intermolecular interactions between a ligand and a target protein. In this study, flexible ligand and rigid protein docking approaches were utilized, employing the 4H3NC molecule as the ligand and targeting human lung cancer protein epidermal growth factor receptor (EGFR) [PDB ID: 2ITO] and human cervical cancer protein p38a Mitogen-activated protein kinase 14 (p38a MAPK) [PDB ID: 3FMK]. The successful docking of the ligand molecule (4H3NC) with the targeted proteins is illustrated in Fig. 12. Dotted yellow lines indicate the formation of hydrogen bonds between the ligand and targeted proteins, along with details on bond lengths and amino acid residues. The title compound has lower binding energy values of −6.66 and −3.65 kcal/mol for the targeted proteins EGFR and p38a MAPK. The inhibitory constants for the HNC-EGFR and HNC-p38a MAPK complexes were found to be 56.14 µM and 113.42 µM.

The results strongly indicate that the 4H3NC molecule exhibits lower binding energy and inhibition constant values specifically for the human lung cancer protein EGFR. These findings imply that the 4H3NC compound might act as a potent inhibitor of the epidermal growth factor receptor. Moreover, these docking results align with the experimental in vitro anticancer findings, further supporting the potential therapeutic efficacy of 4H3NC in combating cancer associated with EGFR.

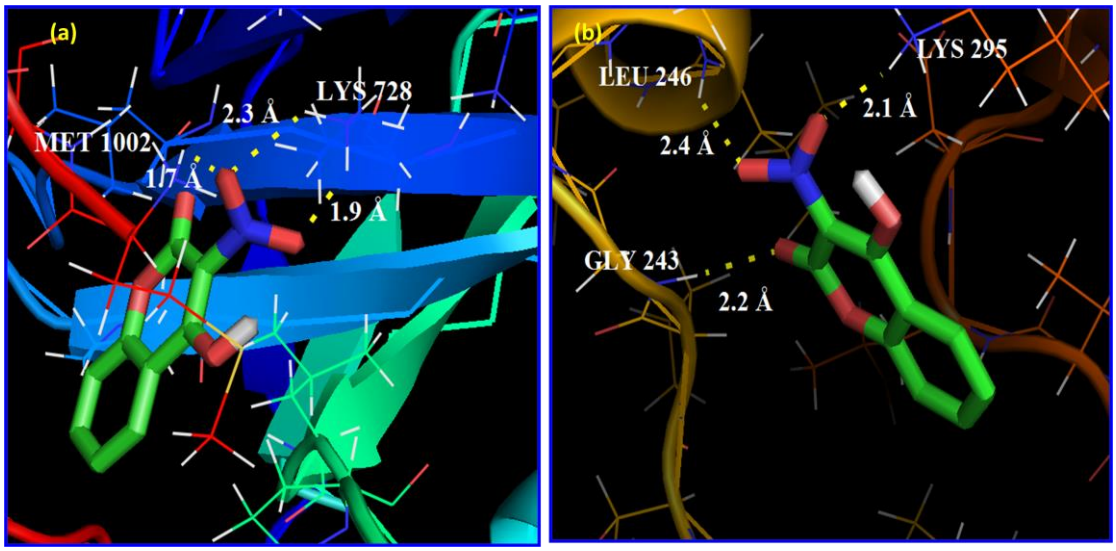

Fig.12. The lowest energy docked poses of the HNC ligand with targeted proteins including (a) EGFR (Epidermal growth factor receptor) and (b) p38a MAPK.

4. Conclusion

The 4H3NC molecule underwent a comprehensive analysis, covering its geometric structure, vibrational assignments, and UV-Visible spectra, revealing distinct electronic transitions crucial for pharmacological applications. Frontier molecular orbitals (FMOs) analysis affirmed its bioactivity through charge transfer, especially via the hydroxyl group's hydrogen atom. MEP surface mapping, Mulliken atomic charge distribution, and NBO investigations concurred, highlighting charge transfer as a key element in the molecule's bioactivity. Antibacterial tests underscored its pronounced inhibitory effect on *Klebsiella pneumoniae* over other strains. In vitro cytotoxicity assays demonstrated the 4H3NC compound's higher efficacy in inhibiting A549 lung cancer cell growth compared to HeLa cervical cancer cells. Additionally, in silico molecular docking elucidated its capacity to impede the function of the epidermal growth factor receptor, notably associated with lung cancer. Collectively, these findings open promising avenues for developing novel drugs targeted at lung cancer treatment.

References

1. Medina FG, Marrero JG, Macías-Alonso M, González MC, Córdova-Guerrero I, Teissier García AG, Osegueda-Robles S (2015) Coumarin heterocyclic derivatives: chemical synthesis and biological activity, Nat Prod Rep. 32(10): 1472-1507.
2. Borges Bubols G, da Rocha Vianna D, Medina-Remon A, von Poser G, Maria Lamuela- Raventos R, Lucia Eifler-Lima V, Cristina Garcia S (2013) The Antioxidant Activity of Coumarins and Flavonoids, Mini-Rev Med Chem. 13(3): 318-334.
3. Joao Matos M, Vazquez-Rodriguez S, Santana L, Uriarte E, Fuentes-Edfuf C, Santos Y (2013) Synthesis and structure-activity relationships of novel amino/nitro substituted 3- arylcoumarins as antibacterial agents, Molecules 18(2): 1394-1404.
4. S.K. Gunduz, Y. Budama Kilinc, B. Bicak, B. Gok, B. Belmen, F. Aydogan, C. Yolacan, New coumarin derivative with potential antioxidant activity: Synthesis, DNA binding and in silico studies (Docking, MD, ADMET), Arab. J. Chem. 16(2) (2023) 104440.
5. G. Pandimeena, R. Premkumar, T. Mathavan, A. Milton Franklin Benial, Spectroscopic, Quantum chemical and Molecular docking Studies on Methyl 6-aminopyridine-3-carboxylate: A potent bioactive agent for the treatment of sarcoidosis, Journal of Molecular Structure 1231 (2021) 129996.
6. Akram N, Mansha A, Premkumar R, Milton Franklin Benial A, Asim S, Zafar Iqbal S, Saqib Ali H (2020) Spectroscopic, quantum chemical and molecular docking studies on 2, 4-dimethoxy-1, 3, 5-triazine: a potent inhibitor of protein kinase CK2 for the development of breast cancer drug, Mol Simul 46: 1340-1353.

7. R. Mohamed Asath, R. Premkumar, T. Mathavan, A. Milton Franklin Benial, Structural, spectroscopic and molecular docking studies on 2-amino-3-chloro-5-trifluoromethyl pyridine: A potential bioactive agent, Spectrochimica Acta Part A 175 (2017) 51-60.
8. M.J. Frisch, et. al., Gaussian 09, Revision C. 02, Gaussian Inc., Wallingford CT, 2009.
9. Gauss View, Version 5, Ray Dennington, Todd Keith and John Milam, Semichem Inc., Shawnee MissionKS, 2009.
10. S. D. Kanmazalp, M. Macit, N. Dege, Hirshfeld Surface, Crystal structure and Spectroscopic Characterization of (E)-4-(diethylamino)-2-((4-phenoxyphenylimino)methyl)phenol with DFT Studies. J. Mol. Struct. 1174 (2018) 133-141.
11. L. J. Bellamy, The Infra-Red Spectra of Complex Molecules, John Wiley and Sons, Inc.: New York, 1975.
12. D. L. Vein, N. B. Colthup, W. G. Fateley, J. G. Grasselli, The Handbook of Infrared and Raman Characteristic Frequencies of Organic Molecules, Academic Press: New York, 1991.
13. S. Premkumar, T. N. Rekha, Beulah J. M. Rajkumar, R. Mohamed Asath, A. Jawahar, T. Mathavan, A. Milton Franklin Benial, Vibrational Spectroscopic and Structural Investigations of 2-Amino-6-Methoxy-3-Nitropyridine: a DFT Approach, Brazilian Journal of Physics 45 (2015) 621–632.
14. R. N. Singh, A. Kumar, R. K. Tiwari, P. Rawat, V. P. Gupta, A Combined Experimental and Quantum Chemical (DFT and AIM) Study on Molecular Structure, Spectroscopic Properties, NBO and Multiple Interaction Analysis in a Novel Ethyl 4-[2-(carbamoyl)hydrazinylidene]-3,5-dimethyl-1H-pyrrole-2-carboxylate and its Dimer, J. Mol. Struct. 1035 (2013) 427–440.
15. M. Anuratha, A. Jawahar, M. Umadevi, V.G. Sathe, P. Vanelle, T. Terme, O. Khoumeri, V. Meenakumari, A. Milton Franklin Benial, Adsorption of N-(1-(2-bromophenyl)-2-(2-nitrophenyl)ethyl)-4-methylbenzenesulfonamide on silver nanoparticles: SERS investigation, Spectrochim. Acta A 138 (2015) 234-240.
16. B. Babu, J. Chandrasekaran, B. Mohanbabu, Y. Matsushita, M. Saravanakumar, Growth, Physicochemical and Quantum Chemical Investigations on 2-Amino 5-chloropyridinium 4-carboxybutanoate – An Organic Crystal for Biological and Optoelectronic Device Applications, RSC Adv. 6 (2016) 110884–110897.
17. S. Chandra, J. Chowdhury, M. Ghosh, G.B. Talapatra, Adsorption of 3-Thiophene Carboxylic Acid on Silver Nanocolloids: FTIR, Raman, and SERS Study Aided by Density Functional Theory, J. Phys. Chem. C 115(29) (2011) 14309–14324.
18. S.K. Gunduz, Y. Budama Kilinc, B. Bicak, B. Gok, B. Belmen, F. Aydogan, C. Yolacan, New coumarin derivative with potential antioxidant activity: Synthesis, DNA binding and in silico studies (Docking, MD, ADMET), Arab. J. Chem. 16(2) (2023) 104440.
19. S. Dhawan, N. Kerru, P. Awolade, A. Singh-Pillay, S.T. Saha, M. Kaur, P. Singh, Synthesis, computational studies and antiproliferative activities of coumarin-tagged 1,3,4-oxadiazole conjugates against MDA-MB-231 and MCF-7 human breast cancer cells, Bioorg Med Chem. 26(21) (2018) 5612-5623.
20. Y. Wang, J. Ai, Y. Wang, Y. Chen, L. Wang, G. Liu, M. Geng, A. Zhang, Synthesis and cMet Kinase Inhibition of 3,5-Disubstituted and 3,5,7-Trisubstituted 29 Quinolines: Identification of 3-(4-Acetylpiperazin-1-yl)-5-(3-nitrobenzylamino)-7-(trifluoromethyl) quinoline as a Novel Anticancer Agent, J. Med. Chem. 54 (2011) 2127- 2142.
21. L.G. Ferreira, R.N. dos Santos, G. Oliva, A.D. Andricopulo, Molecular Docking and Structure-Based Drug Design Strategies, Molecules 20 (2015) 13384-13421.